

Demodulation of a tilted fibre Bragg grating transmission signal using α -shape modified Delaunay triangulation

Fazzi, Luigi; Groves, Roger M.

DOI

[10.1016/j.measurement.2020.108197](https://doi.org/10.1016/j.measurement.2020.108197)

Publication date

2020

Document Version

Final published version

Published in

Measurement: Journal of the International Measurement Confederation

Citation (APA)

Fazzi, L., & Groves, R. M. (2020). Demodulation of a tilted fibre Bragg grating transmission signal using α -shape modified Delaunay triangulation. *Measurement: Journal of the International Measurement Confederation*, 166, Article 108197. <https://doi.org/10.1016/j.measurement.2020.108197>

Important note

To cite this publication, please use the final published version (if applicable). Please check the document version above.

Copyright

Other than for strictly personal use, it is not permitted to download, forward or distribute the text or part of it, without the consent of the author(s) and/or copyright holder(s), unless the work is under an open content license such as Creative Commons.

Takedown policy

Please contact us and provide details if you believe this document breaches copyrights. We will remove access to the work immediately and investigate your claim.



Demodulation of a tilted fibre Bragg grating transmission signal using α -shape modified Delaunay triangulation

Luigi Fazzi*, Roger M. Groves

Structural Integrity and Composites Group of the Faculty of Aerospace Engineering of Delft University of Technology, Delft 2629 HS, the Netherlands



ARTICLE INFO

Article history:

Received 6 March 2020
Received in revised form 22 June 2020
Accepted 5 July 2020
Available online 12 July 2020

Keywords:

Delaunay triangulation
Tilted fiber Bragg grating
FBG
Demodulation
Refractometer
Refractive index

ABSTRACT

Reflective Tilted Fiber Bragg Grating (TFBG) sensors have intriguing sensing capabilities due to the resonance-peaks present in their transmitted spectrum. Previous works measured the external refractive index (ERI) in which the TFBG sensor is placed, by considering the wavelengths or the envelope of the cladding-modes resonances. In this paper, primarily, we demonstrate the effectiveness of an alternative global technique, based on Delaunay triangulation, to analyze the TFBG spectrum for refractometer purposes. Hence, we performed the correlation between the area subtended by the upper and lower cladding-modes peaks and the ERI. An investigation on the goodness-of-fit correlation functions is also presented for TFBG sensors written in standard- and thin-optical fibres and considering different values of the fundamental triangulation parameter α .

© 2020 The Authors. Published by Elsevier Ltd. This is an open access article under the CC BY license (<http://creativecommons.org/licenses/by/4.0/>).

1. Introduction

Short-period gratings with periodicity around 500 nm, otherwise called Fiber Bragg gratings (FBGs), are formed by a permanent modulation of the core of a single-mode (SM) optical fibre (OF). The variation of the refractive index can be imposed with several refractive index profiles along the length of the Bragg grating which modify the propagation of electromagnetic waves inside and, hence, the spectrum of the FBG. Depending on the application of the FBG, uniform, chirped, Gaussian and apodizing are profiles commonly used [1]. In the case of tilted FBG sensors, the previous profile scan is written with a so-called tilt angle with respect to the fibre axis, so that the Bragg gratings are single-sided or, even double-sided tilted [2]. Adjusting the tilt of the gratings, the TFBG transmission spectrum acquires unique features which make it suitable in several applications. Indeed, the detection of the shifting in the spectrum of different peaks allows the separate and simultaneous measurement of strain and temperature at the sensor location [3–7]. Furthermore, the TFBG spectral bandwidth is composed of multiple resonance peaks, called cladding modes, that are more or less sensitive within a determined range of external refractive index (ERI) variations, based on the Bragg grating's characteristics. Therefore, changes of the wavelength and amplitude of

these resonances can be exploited to use the TFBG as a refractometer [8–13]. Also, cladding modes with high effective refractive index are susceptible to macro-bending applied to the OF [14–16]. In other FBG types (such as uniform, chirped, Gaussian and apodizing), cladding resonances are seldom visible in the transmission spectrum; as a well-designed grating keeps the light in the core mode [1,2]. Long Period Gratings (LPG) sensors have been applied for refractometer purposes because their spectrum contains a number of attenuation bands coming from the coupling between the core guided mode and a subset of cladding modes [1]. The resulting peaks are sensitive to external refractive index changes [8], however, as a refractometer, LPGs suffer of some metrological issues, high temperature-strain-bending cross-sensitivity, their grating's length prevents point measurements, short RI sensitivity range and higher cost of the sensor [5,10]. While, in the case of TFBGs, the cross sensitivity is a key point, in fact, a three-parameter optical sensor based on weakly slanted short-period gratings can be developed as the spectral response offers the possibility to considering the shifting of determined peaks and its total transmission power to detect simultaneously strain, temperature and ERI [5,17]. In the last years, attractive sensing abilities have arisen from the embedding of TFBG sensors inside composite materials to monitor their thermo-mechanical deformation state [18,19] and the degree of cure of the resin during the composite manufacturing [20,21]. The interest for refractometers based on TFBGs is also increasing in chemical and biochemical fields, because they offer the possibility of using an optical

* Corresponding author.

E-mail addresses: l.fazzi@tudelft.nl (L. Fazzi), r.m.groves@tudelft.nl (R.M. Groves).

approach to detect chemical and biochemical species without resorting to luminescence- or absorption-based measurements [22,23]. A common application is the measurement of solute concentration in a liquid solution [24,25].

In this work, we propose a new technique based on α -shape modified Delaunay triangulation to demodulate the TFBG transmitted spectrum and perform a correlation with the ERI. The demodulation technique allows the calculation of the envelope area of the upper and lower cladding resonance peaks easily and quickly by considering the TFBG spectrum as a point set for which the Delaunay triangulation is applied. Then, the correlation between the normalized envelope area and the ERI range used during the calibration here performed. Then, we demonstrate that by changing the α -shape value of the triangulation a higher matching can be obtained between the fit functions and the correlation curve.

2. Correlation methods between ERI and TFBG transmission spectrum

Substantially, for refractometric purposes, all the demodulation approaches exploit the correlation between the cladding loss-peaks in the spectrum and the ERI variation. However, a fundamental distinction can be considered between those methods using wavelength-encoded information (wavelength shifting [10] and cutoff resonance [26]), and information contained in transmission spectral changes of the cladding resonances (envelope [8] and area method [17], standard deviation method [24], and contour length approach [27]). These two demodulation classes are respectively called wavelength shift and global methods. Although the wavelength methods are easy to be applied, as they are based on the wavelength shifts of cladding resonances peaks caused by and ERI changes, the use of these techniques would require the temperature and RI sensitivities coefficients of some selected cladding resonances to be known during the calibration step. That makes these techniques sensitive to the cladding resonances to parameters. Moreover, in case of multi-parameter measurements, the coefficients of the sensitivity matrix are fundamental to uncouple opportunely the different perturbations (if the coefficients are close then it is not possible to separate individual effect). The second demodulation group is more suitable for simultaneous multi-parameter measurements because these methods are independent of thermo-mechanical perturbations and they offer precise measurements in a certain ERI range. However, often these approaches have to follow many steps and they are time consuming to perform. In fact, as the spectral peaks of cladding modes are not uniform in amplitude and wavelength distribution, the process of obtaining the envelope of the upper and lower peaks is not always straightforward to perform. In this context, both the envelope curves can be smoother than the spectrum and/or the integral of the transmission, may undergo approximations to better adapt to the mathematical trend. Furthermore, the envelope functions are often generated through piecewise-functions whose integration process is computationally heavy and slow. In this paper we want to introduce a new global approach based on the Delaunay triangulation (also known as Delone triangulation) [28], to calculate the cladding resonances area in the TFBG spectra. This technique is simple and fast to implement, and its performance is independent of the shape of the spectrum of the TFBG. The technique is applied to analyze the cladding resonances of weakly tilted short-period gratings spectra when the sensors were totally surrounded by several liquids with different well-defined refractive indexes (± 0.0002). Hence, the correlation between the spectra and the ERI variations was performed for several values of a fundamental triangulation parameter, the triangulation radius. This approach

allows each minimal variation of shape peaks to be considered (according to the resolution of the interrogator device used to obtain the spectra), and moreover, based on the measuring ERI range, the slope of the correlation curve can be increased so that the resolution of the measurement system to the ERI change increases.

3. Weakly tilted FBG theory and spectrum

In a standard FBG, since the multiplexed gratings are approximately perpendicular to the optical axis of the fibre, coupling is only allowed between the modes propagating inside the core. Specifically, the core forward-propagating light is coupled only with the backward-propagating reflection core mode with a well-defined wavelength determined by the gratings. However, when a tilt angle is imposed, the tilted grating reflects part of the light into the cladding layer of the fibre, where it can be coupled from the cladding modes to the surrounding medium. Hence, a double coupling system occurs inside the core, and in the case of tilt angles $\theta < 45^\circ$, the core forward-propagating mode is also coupled with the core and cladding backward-propagating modes [29]. When the tilt angle reaches a range close to 45° , a great amount of the reflected light in the cladding is irradiated out of the optical fibre, this effect is called radiation mode coupling. The angle range, in which radiation modes are present, depends on a critical angle that can be easily calculated by knowing the cladding and surrounding medium refractive indexes [30]. The radiation mode coupling generates a lack of resonances in the TFBG transmitted spectrum as the cladding modes are no longer guided as they are coupled out from the OF. With a further increase of θ , out of the radiation range, the cladding modes are reflected so that they change their propagation direction from backward to forward and then the coupling with the core mode occurs in this same direction. The coupling modalities influence strongly the transmission spectrum of TFBGs, as well as the tilt angle affecting the coupling between the in-fibre propagating modes, consequently the shape of the TFBG transmission spectrum depends on the value of θ imposed by the Bragg gratings. In this work only weakly tilted FBGs ($\theta < 10^\circ$, also called reflective TFBGs) were used because the unique features of their spectra are more suitable for aerospace applications (for real-time and parallel thermo-mechanical measurements), however the approach introduced below could be applied to any kind of TFBG spectrum.

Inside the TFBG, the light radiation conditions, with varying the tilt angle, can be represented by the core \mathbf{K}_{core} , grating \mathbf{K}_G and radiated \mathbf{K}_R light wave vectors. Specifically, the strongest modes coupling occurs when a phase-match condition is satisfied, which is written as:

$$\mathbf{K}_R = \mathbf{K}_{\text{core}} + \mathbf{K}_G. \quad (1)$$

Since the refractive indices of the core and cladding are similar, we can consider the weakly guided OF approximation to be applicable. As a consequence the amplitudes of \mathbf{K}_{core} and \mathbf{K}_R may be assumed to be approximately the same.

In Fig. 1, δ is the radiation angle, Λ_G is the grating period, Λ is the nominal grating period and θ the tilt angle. From the vector compositions, it is possible to see that, for a tilt angle of less than 45° , the light of the core mode is coupled to the backward-propagating core mode and the cladding modes. \mathbf{K}_R is completely dependent of the inclination of the Bragg gratings. This kind of mode coupling involves special spectral features when the FBG has a tilt angle of less than 10° . Specifically, three main regions can be identified in the spectrum: Bragg peak, Ghost peak, and cladding-mode resonances (Fig. 2).

The Bragg peak is obtained by the same core-core mode coupling that generates the main peak in FBG spectrum. The Ghost res-

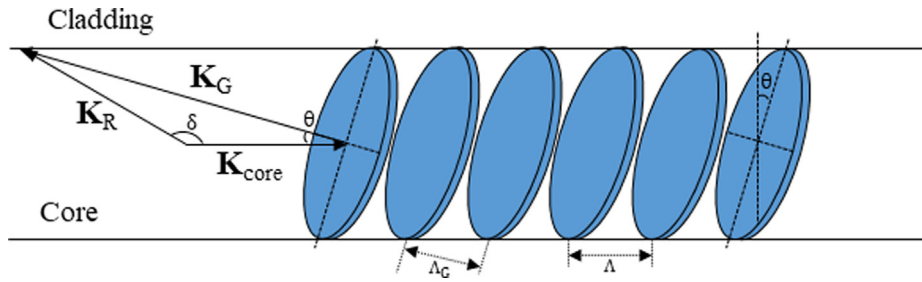


Fig. 1. Phase-matching condition for weakly tilted FBG.

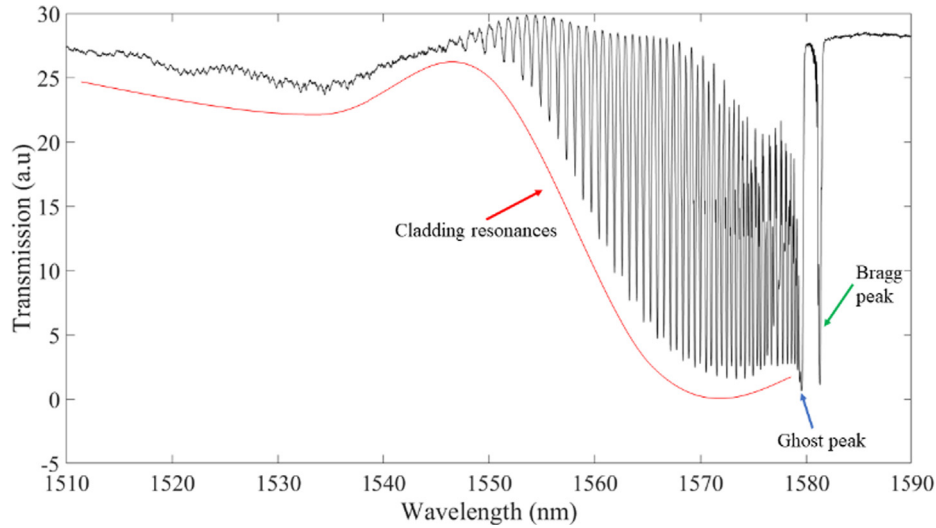


Fig. 2. Bragg, Ghost and cladding resonances in the transmission spectrum of a 5° tilted FBG written in Fibercore SM1500(9/125)P OF.

onance appears in the spectrum slightly away from the Bragg peak, and it is the result of a group of low-order and strongly guided cladding modes coupling with the core light. A possible explanation for why the Ghost peak is single, although the coupling happens between multiple low-order cladding modes, could be that the wavelength resonance of each coupling is near to each other. This means the contribution to the reflection of each of these modes is such that, in transmission, the Ghost peak is a single peak but with larger bandwidth than the other resonances peak (as it is already possible to see in Fig. 2). These Ghost modes have a low interaction with the interface between the cladding and the surrounding as they propagate in a well-confined region of the cladding layer with a strong interaction with the fibre core. The Bragg and Ghost peaks are typically present in the spectrum of FBG with small tilt angles ($\theta < 10^\circ$), however they become invisible for greater grating inclination.

The wavelengths of the Bragg peak and the cladding resonances in the spectrum can be determined by applying the phase-match condition (Eq. (1)) and substituting the parameters characterizing the coupling between the modes. Then, the wavelengths of the Bragg (λ_{Bragg}) peak and cladding ($\lambda_{\text{clad},i}$) resonances are obtained [31]:

$$\lambda_{\text{Bragg}} = 2 n_{\text{eff,core}} \Lambda = 2 n_{\text{eff,core}} \frac{\Lambda_G}{\cos \theta}, \quad (2)$$

$$\lambda_{\text{clad},i} = (n_{\text{eff,core}} + n_{\text{eff,clad},i}) \Lambda = 2(n_{\text{eff,core}} + n_{\text{eff,clad},i}) \frac{\Lambda_G}{\cos \theta}, \quad (3)$$

where $n_{\text{eff,core}}$ and $n_{\text{eff,clad},i}$ are respectively the refractive index of the core and cladding modes. As the above equations show, after the coupling, the spectral position of each resonance is dependent

on the effective refractive index $n_{\text{eff},i}$ of the modes and the tilt angle and period of the gratings Λ_G . Although, all the peaks are sensitive to thermo-mechanical perturbations (the wavelength shifting occurs when a temperature or strain variation is applied to the gratings), in the case of ERI variation, only the cladding resonances are affected by wavelength and amplitude peak loss [8,10]. Indeed, due to the surrounding RI changing, each cladding mode fits to the new condition, propagating with a different effective refractive index. The amplitude of the peaks is also affected when the surrounding RI becomes closer to the effective RI of the i -th mode, these modes become less guided within the cladding and its resonance is weak. While, when the external RI matches the effective RI of i -th mode then the mode is irradiated out and the relative resonance does not appear anymore in the spectrum. Specifically, the i -th cladding mode propagates out from the fibre because, being that the mode and the surrounding medium have the same refractive index, there is no boundary between the two layers and then the internal reflection is missing. Furthermore, the influence of strain and temperature variation on the cladding resonances amplitude and on the RI measuring needs to be considered. As demonstrated in [17,32], although a translation of the whole spectrum is observed with the application of strain to the OF, the area coming from the envelope of the cladding resonances is unaffected, and moreover, the only effect of a temperature variation on spectrum area is generated by the change of the surrounding RI.

This is the physics theory behind the mechanisms that are the basis of the transmitted signal demodulation techniques presented in this section. The new approach, proposed in this paper, exploits the cladding resonances decay and the change in transmitted spectrum shape caused by the ERI effect.

4. Delaunay triangulation

Triangulation methods allow the partitioning of complex polygons into multiple triangles (in 2D) and polyhedrons into tetrahedrons (in 3D), which can then be used to compute the area, volume or to discretize a point set into a convex hull. Other applications in which triangulation is useful are the creation of interpolation functions and the generation of a refined mesh for FEM analysis of complex body parts [28,33]. Several algorithms based on different triangulation strategies have been developed over the years: recursive diagonal insertion, ear cutting, prune and search, decomposition into monotone polygons, divide and conquer, sweep-line, Graham scan, randomized incremental, and using bounded integer coordinates [34]. However, all these algorithms have a common triangulation definition such that the following mathematical conditions are satisfied:

$$\begin{cases} \forall t \in \mathbf{T} \Rightarrow \text{conv}(\mathbf{S}) = \cup t_n, \\ \forall \mathbf{P}_i \in \{\mathbf{S}\} \equiv \mathbf{V}_i, \\ \text{conv}(\mathbf{S}) \cap t_n \equiv \mathbf{V}_i \vee \mathbf{I}_m \vee \emptyset. \end{cases} \quad (4)$$

\mathbf{S} is a set of points, \mathbf{T} is the t_i triangles array or triangulation whole, \mathbf{V}_i and \mathbf{I}_m are the vertices and edges of triangles, while i, m and n are the indices of the relative elements. The first expression in eq.4 describes the convex hull of \mathbf{S} and is the union of all the triangles generated by the triangulation. The second condition in eq.4 establishes each point of \mathbf{S} as a vertex of the generated triangles. The last third condition implies that the intersection between the convolution of the point set and the triangles, generated by the triangulation, coincides with the vertices or the edges of the triangles, or it is empty. Although the previous mentioned strategies may result in a more or less efficient triangulation algorithm, often the obtained triangles are skinny and with long edges. This is undesirable because the triangulation might be non-uniformly distributed, and consequently, the convex hull of the discretized point set may be different from the appropriate one. Indeed, the vertices of some triangles may tend to be spread out from each other or to not be connected properly to each other. Delaunay (D-)triangulation can be considered to avoid these issues and obtain well-shaped and uniformly distributed triangles (Fig. 3) [35]. Starting from Eq. (4), D-triangulation can be defined by adding the so-called empty circum-circle property:

- let $\mathbf{S} = \{P_1(x_1, y_1), P_2(x_2, y_2), \dots, P_i(x_i, y_i)\}$ point set in \mathbb{R}^2 ,
- let $\mathbf{T} = \{t_1, t_2, \dots, t_n\}$ D-triangulation array of \mathbf{S} ,

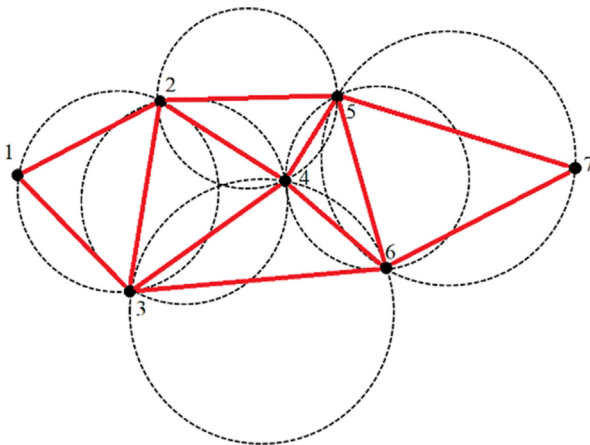


Fig. 3. Delaunay triangulation of a 7 point set.

$$\Rightarrow \forall \mathbf{I}_m \in \mathbf{T} \exists \mathbf{c}_n : \mathbf{I}_m \cap \mathbf{c}_n \equiv \mathbf{V}_i \wedge \mathbf{V}_i \wedge \mathbf{c}_n = \emptyset. \quad (5)$$

where the (x_i, y_i) coordinates are in the plane of several points and \mathbf{c}_n are the circles generated during the triangulation. Briefly, Eq. (5) means for each edge of the triangles generated by the triangulation, a circle exists such that the end of the edges (vertices) are on the boundary of the circle, but at the same time, no other vertex of \mathbf{S} is in the interior of the same \mathbf{c} . When Delaunay triangulation is not applicable then the *constrained* version can be used, where two vertices of the same triangle of \mathbf{T} must be coincident on the boundary of \mathbf{c} and the third can be interior or outside of the circle \mathbf{c}_n [34].

As Fig. 3 shows, each point of the set is a vertex of one or more triangles generated on the circles, and simultaneously, each point is outside by any circle. Moreover, since for three points only one circle can intersect, therefore the written triangle, with vertices the same points, is unique.

5. D-Triangulation demodulation approach

In this section Delaunay triangulation is applied to the TFBG spectrum with the aim of calculating the cladding resonances area, and successively, to correlate it to the external RI variation. For the reasons reported in Section 3, the demodulation technique was applied to the bandwidth corresponding to the cladding resonances and half of the Ghost peak. This choice allows the spectral variations that happen in the bandwidth between the Ghost and the first peak of the cladding resonances to be taken into account. In Fig. 4, the TFBG transmission spectrum is processed as a sequence of points, for which their coordinates in the plane are known, these can be treated as a set \mathbf{S} (Fig. 4).

Each point in the spectrum is potentially a vertex of Delaunay \mathbf{T} . However, if the technique was applied globally to \mathbf{S} then the convex hull, resulting by the triangulation, most likely would be different from the actual envelope of the cladding resonance peaks. Indeed, without a parameter to control the proper connection distance between the vertices, very long edges \mathbf{I} could be generated, by the algorithm, between vertices placed in far bandwidths. This issue can be easily overcome by introducing the notion of α -shape in the algorithm of Delaunay triangulation [36,37]. Substantially, in this way, \mathbf{T} occurs based on the Delaunay definition but, simultaneously, the triangulation is kept under control through the parameter α that represents the r radius of the circles \mathbf{c}_n , and to which can be attributed under different conditions. Specifically, to yield a suitable D-triangulation for our aims, let us consider:

- Delaunay $\mathbf{T} = \{t_1, t_2, \dots, t_n\}$,
- $P_1(x_1, y_1), P_2(x_2, y_2), P_3(x_3, y_3) = \mathbf{V}_i$ (from Eq. (5)),

$$\begin{aligned} \Rightarrow \sqrt{(x_1 - x_r)^2 + (y_1 - y_r)^2} &= \\ = \sqrt{(x_2 - x_r)^2 + (y_2 - y_r)^2} &= \\ = \sqrt{(x_3 - x_r)^2 + (y_3 - y_r)^2} &= r \leq \alpha. \end{aligned} \quad (6)$$

Triangles generated inside circles with $r \leq \alpha$ are allowed by the algorithm, as this allows small variations of the cladding resonances area to be considered and the ‘mesh’ to appear smooth and uniform. During the demodulation phase, we noted that the triangular mesh elements usually have smaller sizes when they are internally used in the convex hull of the spectrum (where the vertices concentration is higher), while longer edges \mathbf{I} are used for the border elements. The α value influences strongly the resulting spectrum triangulation, and, with the aim to calculate accurately the cladding peaks area an optimized value should be applied to perform the discretization.

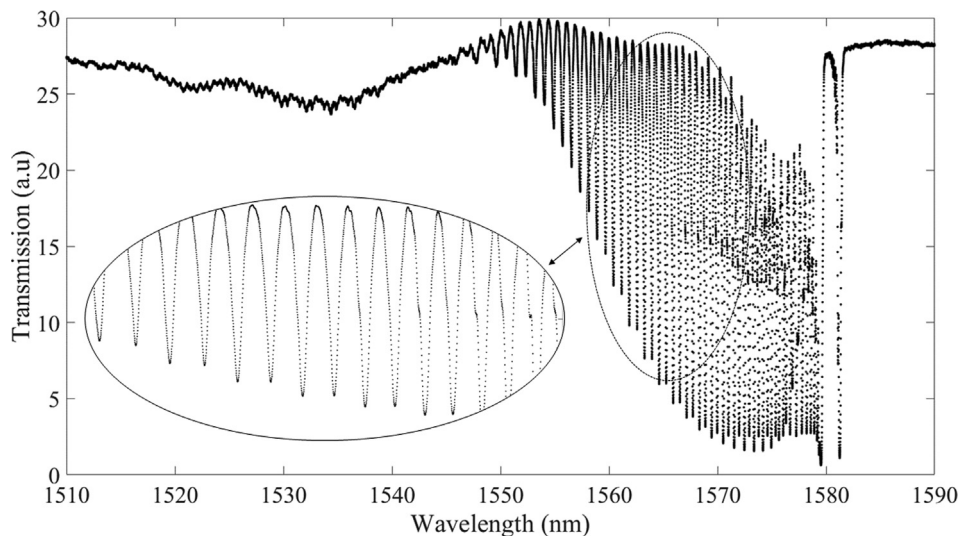


Fig. 4. TFBG transmission spectrum data as a point set.

Fig. 5 shows the D-triangulation of the point set of Fig. 4 performed for several values of α . For α values of 0.1 and 0.5 the triangular elements are not large enough to mesh the entire set point, hence, holes are present. Increasing the maximum permissible radius ($\alpha = 1$), there are no more holes inside convex hull of the spectrum, but the borders do not match smoothly the peaks in some regions.

Increasing again ($\alpha = 2, 6$), the spectrum is perfectly discretized in triangles with a good peaks envelope. In these cases, due to large values of α , some external regions of the spectrum are triangulated as well (as the red arrows indicate in Fig. 5c) and d)). That could seem to be an issue in calculating the resonances area, however, as it will be afterwards demonstrated, it does not influence the success of the correlation. Rather, since these external areas grow and wane congruently with the cladding resonance peaks, a better fitting function of RI correlation might be obtained resulting in a higher predictability and smoother trend of the curve. Obviously not all radii α allow a useful area measurement to be determined, in fact a tradeoff analysis should be performed to select the optimum α , however a radii range exists in which each α value returns anyway an acceptable correlation (see Section 8).

6. Correlation ERI-normalized area

In this work, D-triangulation was applied for the demodulation of tilted FBG spectra written in Fibercore SM1500(9/125)P standard (cladding diameter 125 μm) and thin-single mode OFs (thin-SMF, cladding diameter 80 μm). Sensors were manufactured using the tilted phase mask technique by FORC-Photonics company. The sensors were interrogated with a 4-Channel NI PXI-4844 Universal Input Module based on Fabry-Pérot tunable filter technology able to scan, with 4 pm of resolution, the wavelength range between 1510 nm and 1590 nm. So, by considering the working bandwidth, 20×10^3 points are available for triangulation in the spectrum. A Cargille oils set was used to surround the OF sensor in a well-defined RI environment, the employed liquids had RIs from 1.3 until 1.7 with 0.01 interval and accuracy of ± 0.0002 in the temperature range between 18 and 32 $^\circ\text{C}$. The following results are for a 5 $^\circ$ tilted FBGs, 10 mm sensor length, written in standard and thin-single mode fibre. The coating layer (polyamide) was removed before the experiment to obtain a bare OF for the entire length of the TFBG. The temperature of the immersed sensor was monitored with a K-type thermocouple

and kept at 25 ± 0.75 $^\circ\text{C}$. A digital camera microscope was used to check that no air bubbles remained at the interface between the oil and the cladding of the OF. Moreover, the OF was mounted on a translation stage so that the TFBG sensor can be kept straight during the dipping in a special polycarbonate bowl containing the RI liquids. Once the spectra were acquired via the DAQ system, these were processed by applying the D-triangulation through a dedicated algorithm. Below, considering the TFBG in standard-SMF, three overlapped spectra are reported after the meshing was performed with the sensor surrounded by three oils with different RIs: the red spectrum is for oil with RI = 1.47, in yellow and red when the TFBG is surrounded by a liquid with RI = 1.42, while in the case of RI = 1.33 the spectrum is composed of blue, yellow and red regions. As expected, Fig. 6 shows the reduction of the region formed by the D-triangulation of the cladding resonances as the surrounding refractive index increases. In particular, as reported below, the correlation graph shows, for a refractive index of 1.33, the triangulated cladding area is at its maximum (blue + red + yellow in Fig. 6) and incorporates all the cladding resonances. However, when the ERI grows, the upper and lower relative amplitude peaks fall, hence, for 1.42, the same blue region decreases to the yellow one and then to the red one for 1.47, so that, between the several areas, a ‘funnel effect’ happens. This effect is also visible for higher effective RI cladding modes after zooming into parts of the spectrum as seen in Fig. 7.

Once the spectrum is discretized, the total area can be easily calculated by adding up the areas of all the triangles:

$$\mathbf{A}_T(n) = \sum_{t=1}^m \mathbf{A}_t. \quad (7)$$

From Eq. (7) it is proposed that $\mathbf{A}_T(n)$ is a function of ERI. To investigate this, $\mathbf{A}_T(n)$ for various ERI values is calculated, then the correlation between them is determined. By convention, a normalized area \mathcal{A} is used to create the graph of the TFBG behavior trend with the surrounding RI variation [8]. \mathcal{A} is defined as the ratio between the i -th area and a reference area:

$$\mathcal{A} = \frac{\mathbf{A}_T(n_i)}{\mathbf{A}_T(n_{\text{ref}})} \quad (8)$$

For this work, n_{ref} corresponds to the value obtained for a surrounding RI of 1.33. This choice is arbitrary, however, as n_{ref} has the maximum area, the correlation graph y-axis in Fig. 8 is then between 0 and 1.

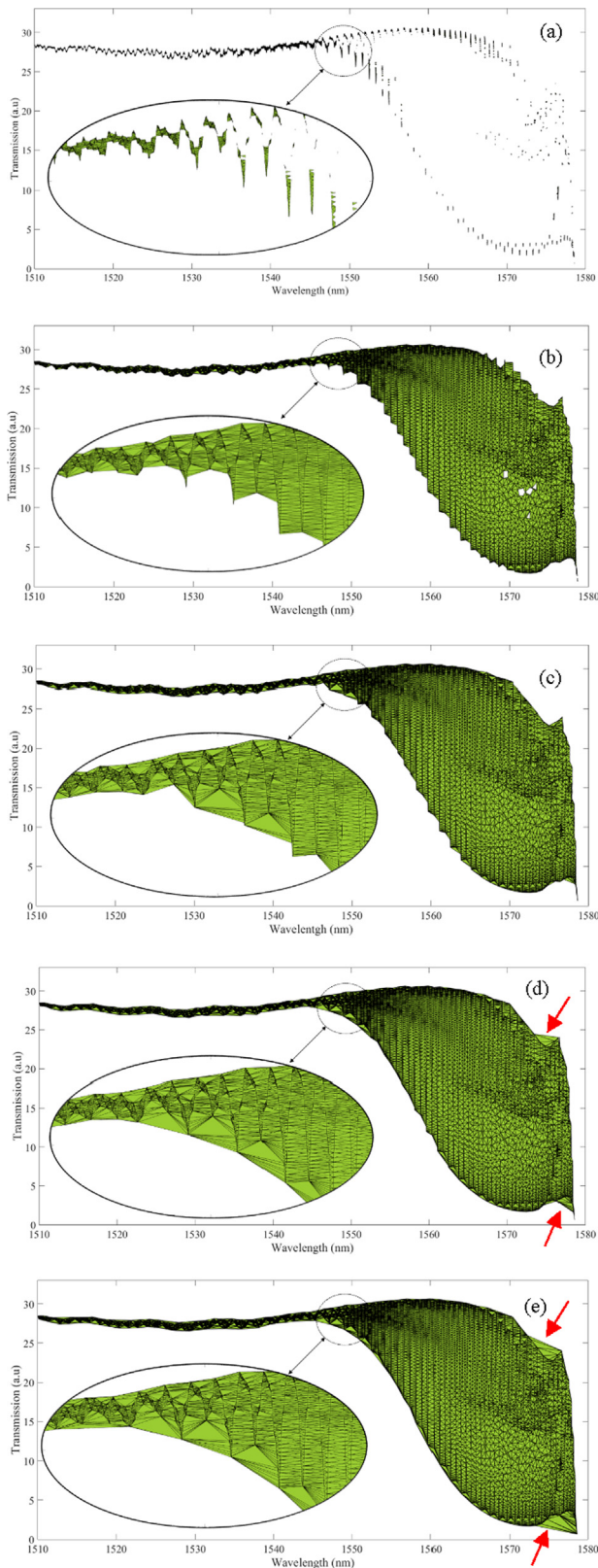


Fig. 5. D-triangulation of 5° tilted FBG transmission spectrum for: a) $\alpha = 0.1$, b) $\alpha = 0.5$, c) $\alpha = 1$, d) $\alpha = 2$ and e) $\alpha = 6$. The red arrows, see text for a detailed description, indicate the triangulation outside the cladding peaks envelope. (For interpretation of the references to colour in this figure legend, the reader is referred to the web version of this article.)

In Fig. 8, the two curves show a different trend although the only parameter that is changing between the TFBG customizations is the cladding diameter of the OF in which the sensors are engraved. From the correlation graph it is possible to deduce some features of the TFBGs spectra and behaviours. Starting from RI = 1, the trend is substantially linear around 1.33 where both curves have their maximum peak. In the said RI range, the same linear trend was detected that was found in previous works [8,38], so it was considered unnecessary to use RIs between 1 and 1.3 for the correlation. In this same range, the red curve (thin-OF) is above the blue curve, as the normalization condition is applied in same way for both the correlations, therefore the ratio \mathcal{A} is bigger for the thin-OF TFBG. Considering that a reduction of the cladding diameter generates an enhancement of cladding mode coupling in TFBG sensors [38], the transmitted resonance peaks of the highest cladding modes (Fig. 9) have a much deeper loss than those recorded for standard OF (Fig. 3). As a possible explanation, for low RI values, is the high cladding mode peaks' contribution to building up the area is greater in the case of TFBG in-thin-OF written than standard waveguides so that the ratio with the maximum area is bigger. Moreover the two lines are not parallel, in particular the red line has a more accentuated slope, this means the susceptibility of cladding modes couplings to ERI is higher in a thin-OF TFBG sensor.

From RI = 1.33 the trend of both curves changes showing the maximum TFBGs sensitivity to the RI variations. Though the standard-OF TFBG is not very sensitive until 1.4, this sensor is highly susceptible to RI variation between 1.4 and 1.46, and its curve has a strong slope. Meanwhile the other sensor exhibits a smooth trend and good slant along the entire range 1.33–1.46. The above description demonstrates how the TFBG sensor customization can influence their sensing abilities. Particularly, in this case, the TFBG in standard-OF is extremely sensitive between 1.42 and 1.46, while the second is susceptible to a more broad range, although having a lower sensitivity.

The last RI interval (1.46–1.7) in our wavelength working window shows substantially the same behavior of both the sensors, which are more or less sensitive to RI changes. Although, the purpose of this work is not to study this behaviour, we tried to explain this phenomenon considering the effect of the internal reflection and the refraction at the interface between cladding and surrounding. When the surrounding RI reaches that of the cladding material all the cladding modes are irradiated out of OF because they propagate as if the two materials are optically the same material. However, by increasing the external RI, the two materials become optically different. In particular, part of the light continues to be irradiated externally, while some modes return to be reflected internally towards the core where they are coupled with the forward-propagating core mode. In fact, in the cladding of the OF, thousands of modes with different effective RIs are present for which the critical angle (or cut-off angle) is not the same, and in particular, when the RI is higher than the cladding RI, some modes are reflected back internally at the cladding-surrounding interface.

Once the correlation curve is obtained with the D-T demodulation technique, a graphics and calculation time comparison with the other methods can be performed. In particular, below in Fig. 10, a graph containing several RI correlation curves obtained by applying the D-T and other demodulation techniques (envelope [8], wavelength shift separation [10] and area method [17]) is reported. Moreover, the necessary times to demodulate a single TFBG transmission spectrum in an auxiliary parameter (normal-

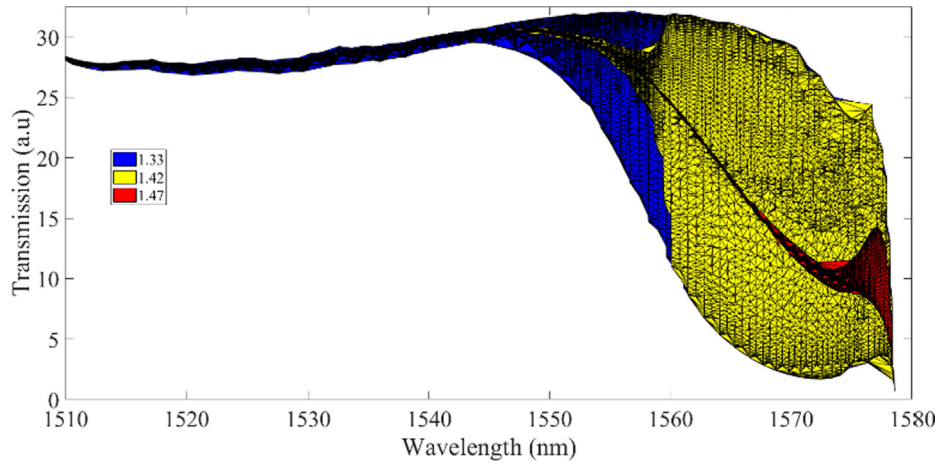


Fig. 6. D-Triangulation of 5° TFBG (in-written standard SMF) spectra immersed in 3 different RI liquids, the imposed α value is 2.

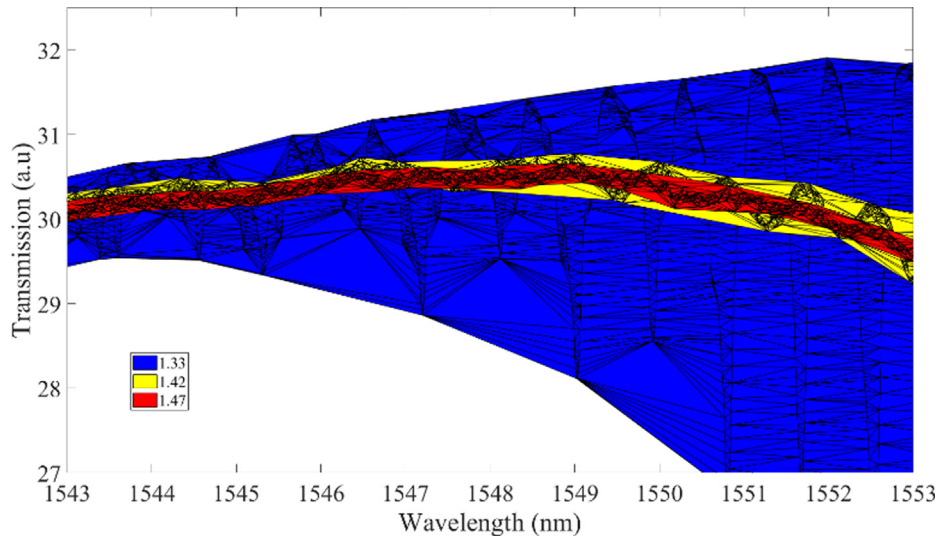


Fig. 7. Triangulated area zoom of medium-high effective RI cladding modes peaks. Also here the 'funnel effect' is visible as smaller ERIs produce greater areas incorporating those obtained for lower ERIs.

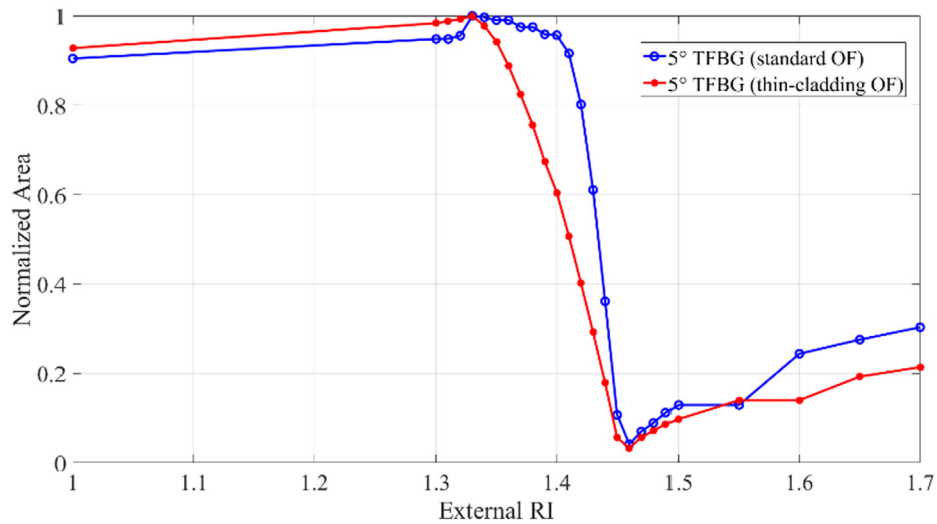


Fig. 8. Correlation ERI-Normalized Area performed through D-triangulation for 5° tilted FBG sensor written in standard (blue curve) and thin-cladding (red curve) OF, $\alpha = 2$. (For interpretation of the references to colour in this figure legend, the reader is referred to the web version of this article.)

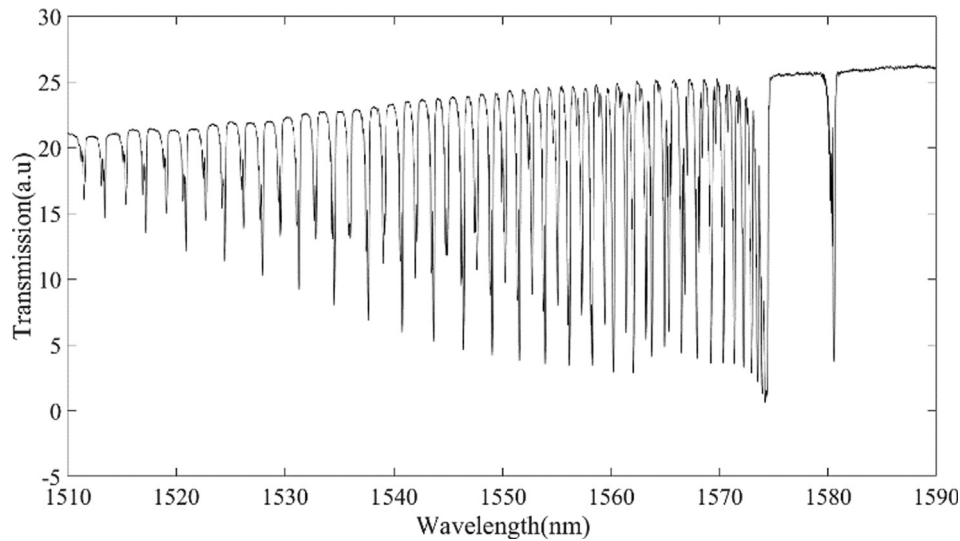


Fig. 9. Transmission spectrum of a 5° tilted FBG written in Fibercore thin-SM1500(9/125)P optical fibre surrounded by air.

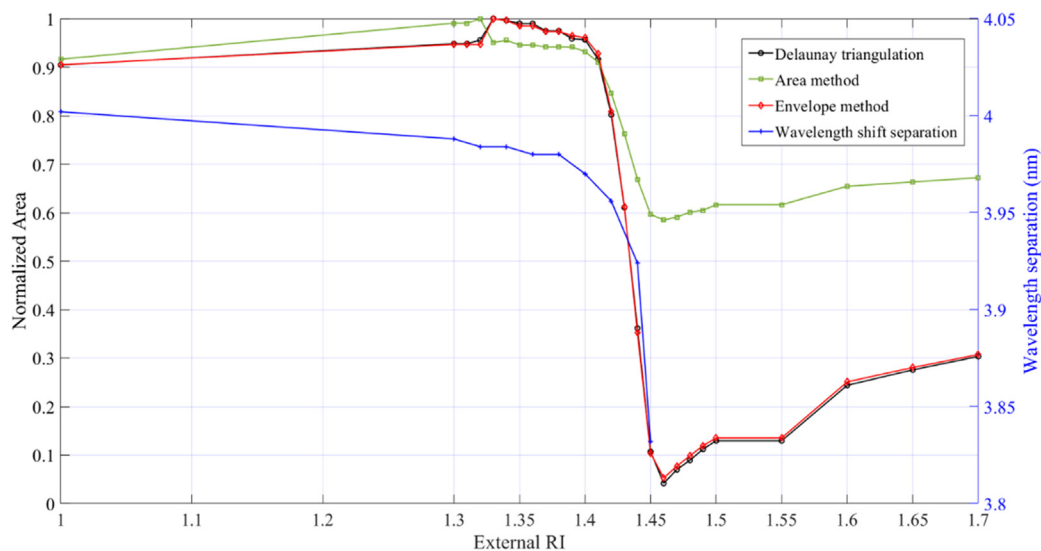


Fig. 10. External RI correlation curves using several demodulation techniques.

ized area or wavelength shift separation) for each used technique are report in Table 1.

From Fig. 10, the envelope and the D-T triangulation techniques provide very close correlation curves, however the area method provides a correlation curve restricted in a smaller range of excursion. The demodulation technique based on the wavelength shift separation develops a correlation curve until 1.45 because the selected peak was recognizable anymore after this RI value. From the times reported in Table 1, the fastest demodulation technique, between the main methods here analysed, is the wavelength shift separation. However, the D-T technique is the fastest of the global

demodulation methods. Although the difference in time between the global techniques could not appear to be relevant, when a high number of spectra have to be demodulated, the difference in processing time-lapse between the techniques becomes important. It is enough to note that the necessary time to demodulate a TFBG spectrum using the Area method is the same as needed by the D-T technique to process more than 16 TFBG spectra. Moreover, the computational time factor is fundamental during the real-time measurement because this value should be smaller than the detection rate of the interrogation system to perform appropriate real-time monitoring.

The wavelength shifting method is faster, however, considering the several drawbacks described in Section 2, the difference in time-lapse is so small to do not justify the use respect the benefits guaranteed by the D-T demodulation technique.

Table 1
Computational times of the analysed techniques to demodulate a single TFBG spectrum.

TFBG demodulation technique	Computational time (sec)
D-T demodulation technique	0.120
Envelope method [8]	1.198
Wavelength shift separation [10]	0.095
Area method [17]	1.998

7. Fitting function of correlation curves

Once the correlation curve has been obtained, it is easy to understand the RI applicability range of the TFBG sensor, or in

other words, where its sensing capability is more effective. However, for practicality, an appropriate fitting function, describing analytically the correlation curve, should be found in the range of interest. That allows the RI value to be obtained directly from the TFBG spectrum area, by solving the equation of the fitting function. However, if a entire RI measurement range is taken into account, then some normalized area values could give two different RIs. This ambiguity may be solved by considering the two statistical parameters Skewness and Kurtosis during the demodulation technique as in [32], as the D-triangulation approach can be used with these statistical parameters, however, this topic is not addressed in this work.

Since the optimum fitting can change based on the RI interval, here, only the best sensitivity RI range is considered. To attribute the goodness-of-fit to each function, the R-square (R^2) statistical approach was used. R^2 , also known as coefficient of determination, is the square of the correlation between the response values and the predicted response values, hence defined as the ratio between the deviation of the regression and the total deviation. R^2 is useful because, being constrained between 0 and 1, it provides an intuitive description of the goodness of the fit. The closer R^2 is to 1, the closer the data points are to the regression line. In this work, we attributed the R-square values to the fitting functions only with the purpose of evaluating the quality of our calibration. The next results show the fitting for the correlation curves of the standard and thin-OF TFBG sensors used in the previous section. Fig. 11 reports a plot of the fitting curves of the correlation points with different polynomial degree along a RI interval).

Though the linear regression is not properly able to represent the correlation trend because the points appear spread out with respect to the regression line, by already considering a quadratic

degree, the fitting function is such that the fitting curve is closer to the data points.

As described above, R^2 allows the quantification of the goodness of fit. In Tables 2 and 3 several R^2 values are reported, taking into account different RI ranges and polynomial degrees of fitting functions. In most of the cases a quadratic function is already enough to match the trend of $\mathcal{A}(\text{RI})$.

Taking into account the resolution of the interrogation system used to detect the TFBG spectra, the resolution of the RI measurement performed through the optical fibre sensor can be calculated. In this case, the NI PXI-4844 interrogator was used to obtain the TFBG spectral responses, which has a scanning wavelength of 4 pm and a power transmission resolution of 4×10^{-6} dB. The minimum detectable variation area is then obtained and, consequently, the minimum variation normalized value respect $A_{T(n_{ref})}$. Considering for both the TFBG sensors, the same RI interval 1.41–1.45 and a triangulation parameter $\alpha = 2$ with the respective linear fitting functions, the obtained RI resolutions for the standard-OF is 3.774×10^{-4} and 3.585×10^{-4} in the case of the thin-OF at 1.44. However, as previous works ([8,17]) have already demonstrated, the resolution can be improved if a better RI reference is taken. Moreover, the resolution can also be improved using a particular α value and, of course, a different fitting correlation function.

At this point, a flow chart is reported below (in Fig.12), as a summary and example of methodology to follow to integrate the algorithms of the here introduced demodulation technique, in a RI measurement system, also considering a possible real-time application.

In the flow chart, the blue arrows show the way the analysis can be performed during the real-time measurements, and it can be noted that this is composed from only 6 steps. The reduction is

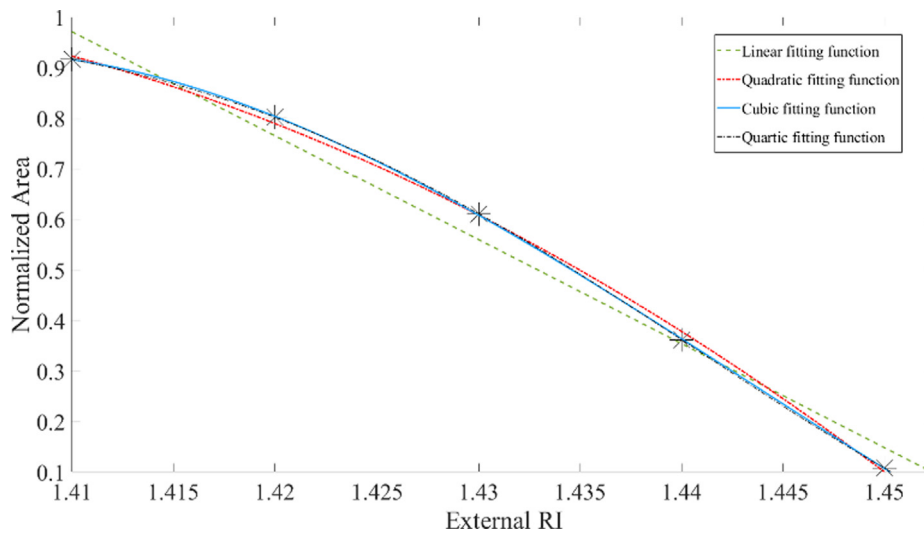


Fig. 11. Fitting of correlation points with several polynomial degrees, standard-OF TFBG sensor.

Table 2

R^2 values of the several fitting curves considering defined RI intervals, correlation curve in the case of TFBG imposed in standard-OF.

RI range	R^2			
	Fitting function degree of $\mathcal{A}(\text{RI})$			
	1	2	3	4
1.40–1.46	0.9625	0.9747	0.9965	0.9998
1.41–1.45	0.9799	0.9988	0.9999	1
1.42–1.45	0.9958	0.9995	1	–

Table 3

R² values of the several fitting curves considering defined RI intervals, correlation curve in the case of TFBG imposed in thin-OF.

RI range	R ²			
	Fitting function degree of \mathcal{A} (RI)			
	1	2	3	4
1.33–1.46	0.9757	0.9953	0.9977	0.9985
1.40–1.46	0.9882	0.9913	0.9973	0.9994
1.41–1.45	0.9991	0.99997	0.99999	1
1.42–1.45	0.9994	0.99997	1	–

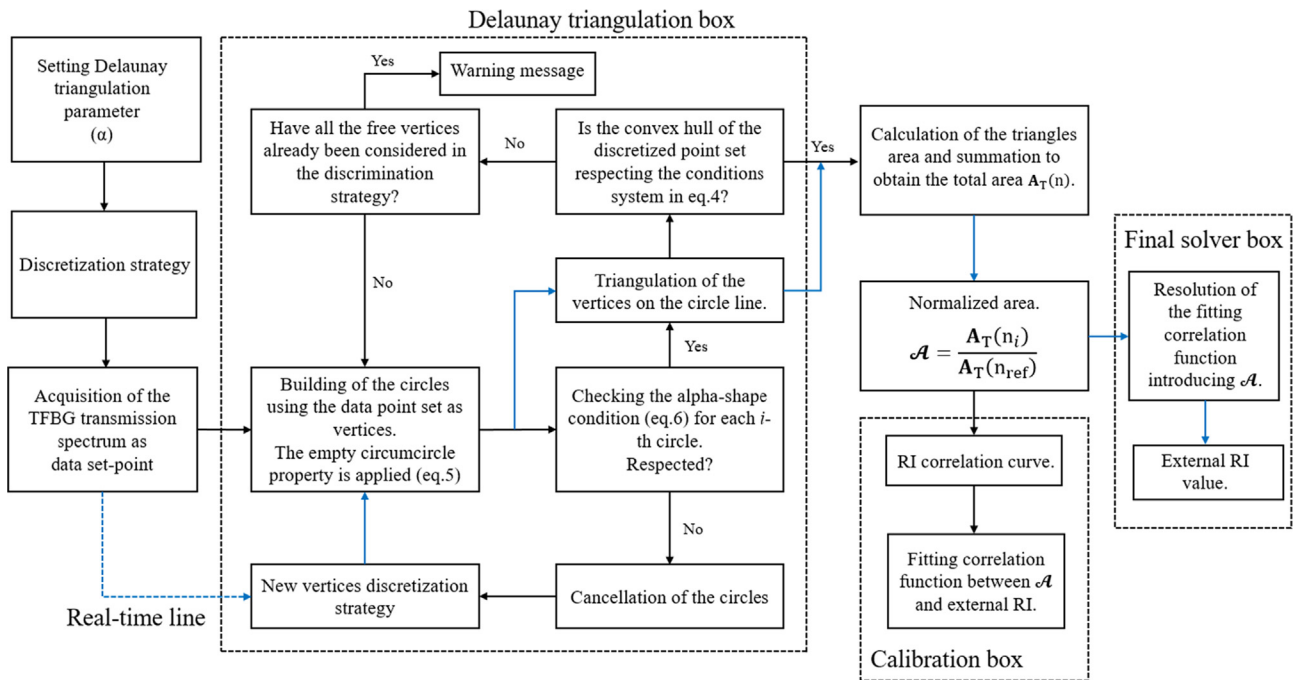


Fig. 12. Flow chart representing the methodology of the D-T demodulation algorithm.

due to the fact the TFBG was calibrated in advance, hence, its measurement algorithm is already optimized for all the RI range. Regarding the discretization or triangulation strategies, as described in Section 4, there are many possible options whose use depends substantially from the programmer; the here reported analysis were performed using the triangulation with divide and conquer method. For real-time application, the discretization in triangles could be performed using a moving and adaptive mesh, this would reduce the triangulation time and speed-up the calculation.

8. Influence of α -parameter on correlation curve

In this section, the problem posed at the end of Section 5, about the influence of the α value used to perform the correlation, is addressed. The first step was to audit the interval of α values in which the correlation curve has a physical meaning. Each correlation curve performed in this work and found in literature for any TFBG customization, is characterized by a slightly increasing upward trend until a maximum point. Then, from this peak, it shows a greater sensitivity RI range with a strong decrease, and from the minimum point the trend becomes again growing. Hence, there are substantially three trend intervals which can be physically justified (Section 3). These trend intervals are expected to remain constant if external disturbances (temperature fluctuations, bending), remain constant. Developing several correlations

with many α values and taking into account the physical meaning above described, two different α intervals were obtained. For the standard-OF TFBG, the suitable interval is $1.6 \leq \alpha \leq 6$, while in the case of the thin-OF TFBG any α greater than 0.8 is useful to perform the demodulation technique. At this point, since the correlation curves keep essentially their same trends, it is not possible to appreciate graphically in detail the differences of using different α values in Fig. 13 and Fig. 14. For this reason, to evaluate how the quality of our RI calibration of TFBGs changes, a study focused on the variation of the R-square value of the fitting functions is necessary. Taking into account some α radii, the same previous fitting function polynomial degrees, and the widest sensitivity RI range of the same TFBGs (in which the correlation curve has the better slope), the calculated R² values are reported in Tables 4 and 5. From the R-square values, it is possible to suppose however that, any α value is suitable to obtain an acceptable fitted correlation curve.

Nevertheless, using a specific α , we can study the fitting quality during the calibration, for example: by considering the TFBG in standard-OF, the best fit for functions of 2- and 3-th order can be obtained using $\alpha = 6$, while in the linear or 4-th order fitting function, the D-triangulation should be performed with $\alpha = 1.6$. For TFBG in thin-OF, an $\alpha = 4$ provides the best fit quality by considering until a 4-th polynomial fitting function. However, when comparing the R-square values in Tables 4 and 5, as mentioned before, the use of another allowable α value does not cause a serious drop in the goodness of the correlation.

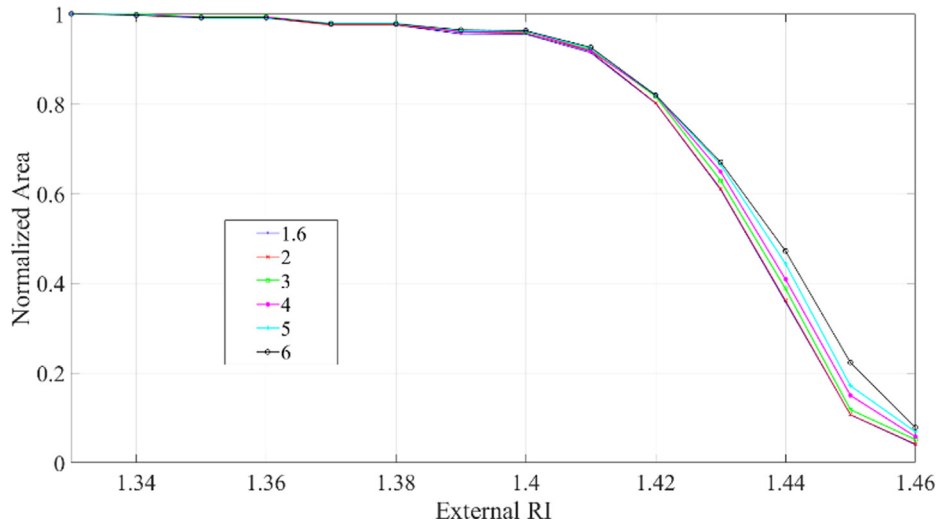


Fig. 13. Correlation ERI-Normalized Area performed with several α values for 5° tilted FBG sensor written in standard OF.

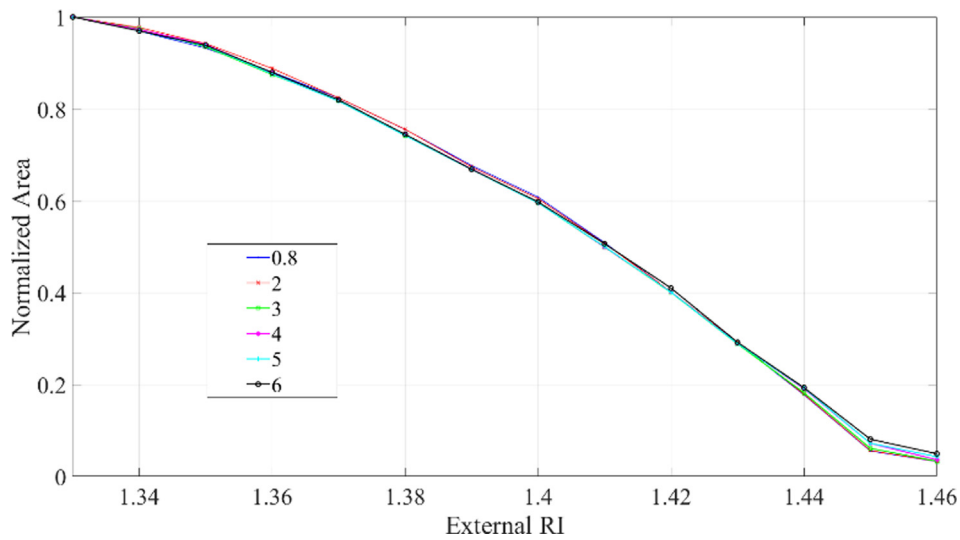


Fig. 14. Correlation ERI-Normalized Area performed with several α values for 5° tilted FBG sensor written in thin-OF.

Table 4
R-square values of several fitting curves in RI interval 1.40–1.46, for TFBG in standard-OF written.

α	R^2			
	Fitting function degree of $\mathcal{A}(RI)$			
	1	2	3	4
1.6	0.96254	0.97474	0.99658	0.99985
2	0.96247	0.97475	0.99651	0.99979
3	0.95871	0.97484	0.99530	0.99955
4	0.95953	0.98015	0.99584	0.99979
5	0.95761	0.98328	0.99533	0.99729
6	0.96172	0.99166	0.99800	0.99939

9. Conclusions

In this study a new concept of demodulation technique for tilted FBG sensors was introduced and demonstrated for refractometric purpose. In principle, the approach is based on the use of Delaunay triangulation to obtain the area of enclosed between the upper and lower peaks of the cladding resonances in the TFBG transmission spectrum, which are correlated to the surrounding RI.

The technique is fast and simple to implement, in fact, the triangulation of the set of input data points from the interrogation of the TFBGs is the unique operating step necessary to obtain the area of the cladding resonances. In this way, the technique does not need the determination of the peaks, the creation of envelope curves and resolution of integrals, or the determination of sensitivity coefficients, saving time and reducing the computational power required. After the spectrum has undergone the meshing, the total

Table 5

R-square values of several fitting curves in RI interval 1.33–1.46, for TFBG in thin-OF written.

α	R^2			
	Fitting function degree of α (RI)			
	1	2	3	4
1	0.97364	0.99526	0.99719	0.99859
2	0.97567	0.99533	0.9977	0.99855
3	0.97887	0.99607	0.99798	0.99874
4	0.97981	0.99643	0.99851	0.99902
5	0.97844	0.99606	0.99821	0.99887
6	0.97976	0.99596	0.99818	0.99886

area is easily calculated by the sum of each area of the triangles created in the spectrum. We demonstrated that this approach can be applied for different kinds of optical fibre in which the TFBG is written, and, there exists always an α range for which the correlation can be performed or rather improved. This demodulation technique can be applied for the analysis of a confined part, or for the total length, of the spectrum, and moreover, since its applicability does not depend on the spectrum shape, it can be used in any kind of TFBG customization. Potentially, these features allow this approach to be also exploited for real-time spectrum monitoring with a moving mesh, and this demodulation method is besides compatible with other techniques for simultaneous multiple measurements. Furthermore, in both the case of real-time measurements or data post-processing, when the spectrum is affected by some disturbances like connectors power losses or bending of the optical fibre, for which the TFBG signal could present some ripples, this approach should be able to operate without particular issues being insensible to the spectrum shape and power loss. In this paper, the technique was applied substantially to correlate part of the power transmitted by the TFBG with the surrounding refractive index, however, the same may be used in all the case where a power contained in a signal needs to be converted or correlated to another significant parameter. An immediate future research objective is a work focused on multi-parameter sensing using the demodulation technique based on the D-triangulation technique.

CRedit authorship contribution statement

Luigi Fazzi: Resources, Conceptualization, Methodology, Software, Formal analysis, Data curation, Investigation, Writing - original draft, Visualization. **Roger M. Groves:** Conceptualization, Methodology, Resources, Validation, Writing - review & editing, Supervision, Visualization, Project administration.

Declaration of Competing Interest

The authors declare that they have no known competing financial interests or personal relationships that could have appeared to influence the work reported in this paper.

Acknowledgement

We would like to thank our colleague Dmitrii Klyukin for his contribution in choosing the best TFBG sensor customization, and his comments and suggestions during the preparation of this paper. This research was supported by the Operationeel Programma Zuid-Nederland (Op-Zuid) Project as part of the Dutch Composite Maintenance Centre (DCMC), supported by the European Fonds voor Regionale Ontwikkeling (EFRO).

References

- [1] T. Erdogan, Fiber grating spectra, *J. Light. Technol.* 15 (8) (1997) 1277–1294.
- [2] K.S. Lee, T. Erdogan, Fiber mode conversion with tilted gratings in an optical fiber, *Opt. Soc. Am.* 18 (5) (2001) 1176–1185.
- [3] E. Chehura, S.W. James, R.P. Tatam, Temperature and strain discrimination using a single tilted fibre Bragg grating, *Opt. Commun.* 275 (2007) 344–347.
- [4] Y. Miao, B. Liu, C. Zhao, Simultaneous measurement of strain and temperature using single tilted fibre Bragg grating, *Electron. Lett.* 44 (21) (2008) 1242–1243.
- [5] X. Dong, H. Zhang, B. Liu, Y. Miao, Tilted fiber Bragg gratings: principle and sensing applications, *Photonics Sensors* 1 (1) (2010) 20–21.
- [6] S. Rahimi, D. Ban, G. Xiao, Z. Zhang, J. Albert, Temperature and strain sensors based on integration of tilted fiber bragg gratings with a free spectral range matched interrogation system, *Sensors J.*, IEEE 9 (7) (2009) 858–861.
- [7] M. Amanzadeh, S.M. Aminossadati, M.S. Kizil, A.D. Rakić, Recent developments in fibre optic phase sensing, *Measurement* 128 (2018) 119–137.
- [8] G. Laffont, P. Ferdinand, Tilted short-period fibre-Bragg-grating-induced coupling to cladding modes for accurate refractometry, *Meas. Sci. Technol.* 12 (2001) 765–770.
- [9] M.S.D. Chun-Liu Zhao, Xiufeng Yang, W. Jin, Simultaneous temperature and refractive index measurements using a 3° slanted multimode fiber Bragg grating, *J. Light. Technol.* 24 (2) (2006) 879–883.
- [10] C. Chan, C. Chen, A. Jafari, A. Laronche, D.J. Thomson, J. Albert, Optical fiber refractometer using narrowband cladding-mode resonance shifts, *Appl. Opt.* 46 (7) (2007) 1142–1149.
- [11] Y. Miao, B. Liu, S. Tian, Q. Zhao, Temperature-insensitive refractive index sensor based on tilted fiber Bragg grating, *Microwave Opt. Technol. Lett.* 51 (2) (2009) 479–482.
- [12] T. Wang, K. Liu, J. Jiang, M. Xue, P. Chang, T. Liu, Temperature-insensitive refractive index sensor based on tilted moiré FBG with high resolution, *Opt. Express* 25 (13) (2017) 14900–14909.
- [13] Y.C. Lu, R. Geng, C. Wang, F. Zhang, C. Liu, T. Ning, S. Jian, Polarization effects in tilted fiber bragg grating refractometers, *J. Light. Technol.* 28 (11) (2010) 1677–1684.
- [14] S. Baek, Y. Jeong, B. Lee, Characteristics of short-period blazed fiber Bragg gratings for use as macro-bending sensors, *Appl. Opt.* 41 (4) (2002) 631–636.
- [15] Y.X. Jin, C.C. Chan, X.Y. Dong, Y.F. Zhang, Temperature-independent bending sensor with sensor with tilted fiber Bragg grating interacting with multimode fiber, *Opt. Commun.* 282 (2009) 3905–3907.
- [16] Q. Wang, Y. Liu, Review of optical fiber bending/curvature sensor, *Measurement* 130 (2018) 161–176.
- [17] N.J. Alberto, C.A. Marques, J.L. Pinto, R.N. Nogueira, Three-parameter optical fiber sensor based on a tilted fiber Bragg grating, *Appl. Opt.* 49 (31) (2010) 6085–6091.
- [18] P. Ferdinand, S. Magne, V. Dewynter-Marty, S. Rougeault, L. Maurin, Applications of fiber Bragg grating sensors in the composite industry, *MRS Bull.* (2018) 400–407.
- [19] D. Kinet, D. Garra, P. Mégret, C. Caucheteur, Temperature and strain effects discrimination inside composite materials with embedded weakly tilted fibre Bragg grating, *Proc. SPIE*, 8794 (2013) 87942R1–87942R6.
- [20] G. Rajan, B.G. Prusty, Structural Health Monitoring of Composite Structures Using Fiber Optic Methods, CRC Press, 2003, pp. 238–243.
- [21] S.J. Buggy, E. Chehura, S.W. James, R.P. Tatam, Optical fibre grating refractometers for resin cure monitoring, *J. Opt. A: Pure Appl. Opt.* 9 (2007) S60–S65.
- [22] F. Baldini, M. Brenci, F. Chiavaioli, A. Giannetti, C. Trono, Optical fibre gratings as tools for chemical and biochemical sensing, *Anal. Bioanal. Chem.* 402 (2012) 109–116.
- [23] T. Guo, F. Liu, B.O. Guan, J. Albert, Tilted fiber grating mechanical and biochemical sensors, *Opt. & Laser Technol.* 78 (2016) 19–33.
- [24] L.B. Melo, J.M. Rodrigues, A.S. Farinha, C.A. Marques, L. Bilro, N. Alberto, J.P. Tomé, R.N. Nogueira, Concentration sensor based on a tilted fiber Bragg grating for anions monitoring, *Opt. Fiber Technol.* 20 (2014) 422–427.
- [25] C. Caucheteur, F. Lhomme, K. Chah, M. Blondel, P. Megret, Use of tilted Bragg gratings to simultaneously measure sugar concentration and temperature during the production process of sugar, *Proc. SPIE* 5855 (2005) 451–454.

- [26] F. Liu, T. Guo, J.G. Liu, X.Y. Zhu, Y. Liu, B.O. Guan, J. Albert, High-sensitive and temperature-self-calibrated tilted fiber grating biological sensing probe, *Chin. Sci. Bull.* 58 (21) (2013) 2611–2615.
- [27] S. Gieszczyk, D. Harasim, P. Kisala, A novel simple TFBG spectrum demodulation method for RI quantification, *IEEE Photonics Technol. Lett.* 29 (24) (2017) 2264–2267.
- [28] D.T. Lee, A.K. Lin, Generalized Delaunay triangulation for planar graphs, *Discrete Comput. Geom.* 1 (1986) 201–217.
- [29] C. Caucheteur, D. Paladino, P. Pilla, A. Cutolo, S. Campopiano, M. Giordano, A. Cusano, P. Mégret, External refractive index sensitivity of weakly tilted fiber Bragg gratings with different coating thicknesses, *IEEE Sensors J.* 8 (2008) 1330–1336.
- [30] K. Zhou, L. Zhang, X. Chen, I. Bennion, Low thermal sensitivity grating devices based on ex-45° tilting structure capable of forward-propagating cladding modes coupling, *J. Light. Technol.* 24 (2006) 5087–5094.
- [31] K.S. Lee, T. Erdogan, Fiber mode coupling in transmissive and reflective tilted fiber gratings, *Appl. Opt.* 39 (9) (2000).
- [32] C. Caucheteur, P. Mégret, Demodulation technique for weakly tilted fiber Bragg grating refractometer, *IEEE Photon. Technol. Lett.* 17 (12) (2005).
- [33] J.R. Shewchuk, Delaunay refinement algorithms for triangular mesh generation, *Computat. Geometry* 22 (2002) 21–74.
- [34] M. Lamot, B. Zalik, An overview of triangulation algorithms for simple polygons, in: *IEEE Intern. Confer. On Inf. Visual.*, London, UK, 2002, doi:10.1109/IV.1999.781552.
- [35] L.P. Chew, Constrained delaunay triangulations, *Algorithmica* 4 (1989) 97–108.
- [36] H. Edelsbrunner, D.G. Kirkpatrick, R. Seidel, On the shape of a set points in the plane, *IEEE Trans. Inform. Theory IT-29* (4) (1983).
- [37] H. Edelsbrunner, E.P. Mücke, Three-dimensional alpha shapes, *ACM Trans. Graphics* 13 (1) (1994).
- [38] C. Caucheteur, K. Chah, F. Lhommé, M. Debliquy, D. Lahem, M. Blondel, P. Mégret, Enhancement of cladding modes couplings in tilted bragg gratings owing to cladding etching, *Proc. IEEE/LEOS* (8531806) (2005).